International Journal on Advanced Science Engineering Information Technology

Vol.14 (2024) No. 2
ISSN: 2088-5334

Effect of Heat Source on the Formation of Welding Zone Structure between Carbon Steel and Stainless Steel Applied in Shipbuilding

Thi Nhung Le [a], Anh Tuan Vu [b], Huu Cuong Le [c], Van Huong Dong [d], Van Phuc Nguyen [c], Thanh Nam Dang [c,*]

[a] *School of Mechanical Engineering, Vietnam Maritime University, Haiphong, Vietnam*
[b] *Faculty of Basic-Fundamental Sciences, Vietnam Maritime University, Hai Phong City, Vietnam*
[c] *Institute of Maritime, Ho Chi Minh City University of Transport, Ho Chi Minh, Vietnam*
[d] *Institute of Mechanical Engineering, Ho Chi Minh City University of Transport, Ho Chi Minh, Vietnam*
*Corresponding author: *nam.dang@ut.edu.vn*

***Abstract*— This work presents the influence of heat sources on forming the weld zone structures between carbon steel and stainless steel. The results show that the weld structure includes the melting, transition, and heat-affected zones. The microstructure on the stainless-steel side is in the form of δ-Ferrite with thin fibers and clusters of Widmantes Austenite formed due to the high cooling rate in this area. On the carbon steel side, the influence of the concentration gradient and cooling rate changes the crystallization pattern from A-A-FA. The structure obtained from the melting boundary is a completely Austenite to Austenite + δ-Ferrite zone with δ-Ferrite varying from cylindrical, dendritic, and axial crystal forms. The δ-Ferrite content is inversely proportional to the hardness. In the melting zone, the change in the ratio value between temperature gradient and crystallization rate is the cause of the change in δ-Ferrite in this region. The HAZ region has Widmanstet phases, Bainite, and Martensite, which are phases with high hardness and brittleness. This area is thus easily destroyed. The results on the microhardness of the weld in the transition zone on the carbon steel side show that the microhardness result is 390HV in the fusion boundary area, the hardness value in the weld metal area ranges from 160 to 173HV, and the primary metal hardness value of carbon steel is from 134 to 146HV.**

***Keywords*— Weld area; transition zone; heat-affected zone; Ferrite; Widmanstet Austenite; Baitite; Martensite.**

Manuscript received 15 Dec. 2023; revised 19 Feb. 2024; accepted 15 Mar. 2024. Date of publication 30 Apr. 2024.

I. Introduction

Nowadays, materials are developing to satisfy the ever-increasing demand for industrial manufacturing, including electrical-electronic field, shipbuilding, mechanical engineering, and buildings [1–7]. Material development mainly focuses on searching for new materials with low cost and high efficiency, solutions to material treatment, and enhancing the mechanical properties of materials [8–15]. Among these, welding produces most steel structures in engineering industries. Welding brings many advantages, such as not simple technology, low production costs, and high welding efficiency [16–19]. Especially welding between different materials such as stainless steel with carbon steel, stainless steel with copper, copper alloy, heat-resistant steel with stainless steel, titanium, and steel is increasingly being applied in many industries such as the chemical industry, mechanical engineering, shipbuilding, and aerospace due to the ability to combine good properties of different materials for each location and other mechanical engineering parts [20–22]. However, one of the main difficulties in welding dissimilar materials using the fusion welding method is the formation of large amounts of intermetallic phases as well as the differentiation of weldment regions [23–25].

Many scientific studies have shown that the influence of the distribution of intermetallic phases and the division of structure regions dramatically affects the mechanical properties of the weld [26–31]. Intermetallic phases have destructive properties, such as high brittleness or the heat-affected zone of the weld, which is a place with low mechanical properties. Cracks often appear, destroying the weld [32–34]. Fusion welding methods have high flexibility in weld configuration and high welding productivity and are widely used in joining dissimilar materials [35,36]. However, it isn't easy to obtain a good weld when directly welding these materials, especially between steel and copper, because of the formation of intermetallic phases and the thermal control of the conductive weld temperature field [37–40]. This leads to the welding heat-affected zone (HAZ) formation, which increases the possibility of weld cracking [41–43]. Chen et al. [44] reported higher weld tensile strength when laser welding with the laser beam shifted toward stainless steel. Some previous studies have shown that intermediate layers can effectively change the phase composition and suppress the intermetallic phase formation reactions. As reported, the Cu interlayer can limit the diffusion of Ti into the molten zone, and no formation of $TiFe_2$ takes place at the interface between the molten zone and the steel [45]. The V element shows good bonding with neighboring materials in dissimilar welds between Ti-Fe [46]. Atomic diffusion and migration between Ti and Fe or C were effectively prevented by adding pure Ni as the interlayer metal, and a strong weld was obtained [47]. Therefore, an intermediate layer can limit atomic diffusion to prevent the formation of brittle IMCs and the formation of some other IMCs. Tomashchuk et al. [48] described that beam deflection dramatically affects the mechanical properties. They reported that the electron beam shifted toward the steel, and the Cu interlayer could inhibit the melting of the titanium alloy and the formation of brittle Fe-Ti phases. A maximum tensile strength of 350 MPa was achieved with a diffusion path length of 40-80 µm of Ti. Hao et al. [49] found a Ti/Cu reaction zone formed between the TC_4 substrate and the solder joint using copper-based filler wire, FeTi and Fe_2Ti compounds were also generated with increasing welding heat input. However, all joints broke at the Ti/Cu reaction zone due to the brittleness of natural Ti-Cu phases. According to the Ti-Cu and Cu-Fe binary phase diagrams, different Ti/Cu brittle phases are formed at the diffusion transition zone; however, the microstructure of the Cu-Steel interface is mainly solid solvent phases. The study of Yao et al. [50] stated that solid solution phases have more properties than brittle intermetallic phases.

Cao et al. [44] Zhao et al. suggested that the CMT method could achieve excellent Ti/Cu joints, and all joints fractured in the HAZ of Cu with ductile fracture mode. This indicates that a layer of intermetallic compounds with 120 µm is controlled with different ring configurations. Studying laser welding between Ti and Cu, Zhao et al. [51] It was found that an intermetallic layer about 25 µm thin was formed between the weld metal and the Ti substrate, with the laser shifting to Cu. Intermetallic compounds such as TiCu, $TiCu_2$, Ti_2Cu, and Ti_3Cu_4 are formed and considered the bond's weakest region. Chen et al. [52] studied Cu-steel welds by laser welding, and the results showed that the tensile strength depends weakly on the melting of Cu. Magnabosco et al. [53] joined a Cu plate to three different stainless-steel plates and showed a complex heterogeneous fusion zone microstructure characterized by rapid cooling and poor material mixing. The transition zone contains significant elements that are insoluble in each other. Besides, the joint shape can increase the effective bonding area and improve the welding quality. The wetting and spreading ability of molten metal plays a vital role in the morphology of the weld. Dual electrode gas metal arc pulse for welding Al and galvanized mild steel and found that alternating transfer of droplets can improve the wettability of molten aluminum [54]. The magnetic field affected the flowability and surface spreading ability of the molten filler metal on the TA_2 plate, thus improving the wetting behavior. [55]. Effect of heat input on the microstructure of Al/Cu joints using low heat input dual electrode gas arc welding [56]. A quadratic relationship between the IMC layer thickness and the welding heat input is derived using the theory of the thermal activation process. Besides, the variable droplet transfer process can affect the weld formation process. Studying the impact of Zn coating on the wetting process of liquid droplets by Cao et al. [57] revealed that the evaporation of Zn can reduce the temperature at the contact surface and expose new metals to the steel surface.

The input temperature dramatically influences the difference in structure zone division in the weld [58,59]. The correlation between the temperature of the solder and time can be expressed theoretically through heat transfer analysis during the welding process. The heat transfer of solder includes many complex phenomena such as convection, radiation, heat conduction, and movement of liquid metal flow [60–66]. Understanding this process requires solving heat transfer differential equations using numerical methods such as finite differences or finite elements with computer software [67–74]. The heat transfer process here can be divided into two stages: the first stage considers the characteristics of the welding arc and the movement of particles in the liquid metal droplet from the moment of formation until impact with the bare metal; the second stage is the heat transfer process from the heat source (center of the weld) to the surrounding environment [75,76]. This work summarized research results on the influence of the mixture of elements in the forming process of the weld area and the influence of the heat transfer process on weld formation.

II. Materials and Method

A. Prepare Welding Samples and Welding Procedures

Stainless and carbon steel are cut on a wire cutter to create panels measuring 275x85x3 mm. The samples are ground clean at the weld seam to remove surface impurities and avoid possible defects. Because the samples are thin, there is no need to perform chamfering. After that, the panels are welded and fixed at both ends. In this experiment, an arc welding machine welds stainless steel with carbon steel. Welding electrode: 304 austenitic stainless steel and carbon steel are welded using a 3mm E309L-16 electrode. Before welding, the electrode must be dried to avoid defects caused by moisture. Table I gives the chemical composition of the base metal and electrode metal.

TABLE I
CHEMICAL COMPOSITION OF BASE METALS AND ELECTRODE METALS

Element	C [%]	Mn [%]	Si [%]	S [%]	P [%]	Cr [%]	Ni [%]	Mo [%]	V [%]
Austenitic stainless steel 304	0.09	1.54	0.49	0.005	0.005	18.3	7.56	0.13	0.11
Carbon steel	0.18	0.62	0.02	0.04	0.05	0.02	0.08	0.005	0.01
E309L – 16 welding electrodes	0.03	1.34	0.71	0.005	0.003	23.7	12.6	-	-

After preparation, the steel samples are welded together using the SMAW method. Welding modes are given in Table II.

TABLE II
WELDING MODE

Welding parameters	I (A)	U (V)	V (mm/ph)	Environmental temperature (^{0}C)
Values	80	25	100	30

B. Experimental Method of Analyzing Welded Joints

Optical methods, scanning electron microscope: Samples measuring 20x10x3mm were cut on the weld cross-section to prepare for the testing process. The sample preparation is performed sequentially from grinding, polishing, and etching. First, the sample is sanded on sandpaper 100, 200, 400, 600, 800, 1000, 1200, 1500, and 2000 so that the surface is shiny and free of scratches. Then, polish on a Struers machine using 5µm Al2O3 grinding powder. Finally, the sample was etched with an etching solution, as shown in Table III. The microstructure was captured using a Leica 4000 optical electron microscope and a FESEM (Field Emission Scanning Electron Microscopy) scanning electron microscope.

TABLE III
ETCHING SOLUTION PROPERTIES

Materials	Austenitic stainless steel 304	Welding metal	Carbon steel
Etching solution type	5g $FeCl_3$ + 15cm^3 HCl + 50cm^3 H_2O	5g $FeCl_3$ + 15cm^3 HCl + 50cm^3 H_2O	3% HNO_3

EDS analysis determines the number of alloying elements at a point or line. EDS-line is used at the fusion boundary on the carbon steel side and the stainless steel side after welding and after heat treatment to determine the concentration distribution curve of alloying elements in this region, especially the concentration of carbon, to determine the ability of carbon to diffuse from carbon steel to weld metal. Point EDS is performed to determine the chemical composition of the carbide particles formed in the weld.

C. Determination of microhardness

Microhardness was determined for the samples after welding and after heat treatment. Microhardness was performed on a Galileo hardness tester with a measuring load of HV0.05. Measure microhardness at the following locations:

- From the carbon steel molten border to the two sides are the carbon steel HAZ region and the weld metal region. The distance between measurement marks near the border is 10 - 20µm to determine the change in microhardness due to the influence of carbon diffusion from the HAZ region of carbon steel to the weld metal region.
- Measure points at the center of the weld metal.
- From the stainless-steel molten border to both sides are the HAZ region of stainless steel and the weld metal region; γ

III. RESULTS AND DISCUSSION

A. Blending and zoning of the weld

Austenitic stainless steel is a type of steel widely used in practice with a basic composition of high Cr and Ni content. The microstructure of stainless steel is γ as shown in Fig. 1a. The carbon steel used has a low carbon content of about 0.18%. The microstructure of the carbon steel, as shown in Fig. 1b, includes clusters of pearlites (black area) and ferrite (white area) with pearlite content of about 22.5% (calculated according to the Fe-C state diagram). Major elements such as carbon (C), silicon (Si), manganese (Mn), vanadium (V), and chromium (Cr) are known to significantly influence mechanical properties and microstructure in the weld between carbon steel and stainless steel. For example, the formation of a refined grain structure is attributed to the presence of Mn and V, while carbide formation is due to the presence of C.

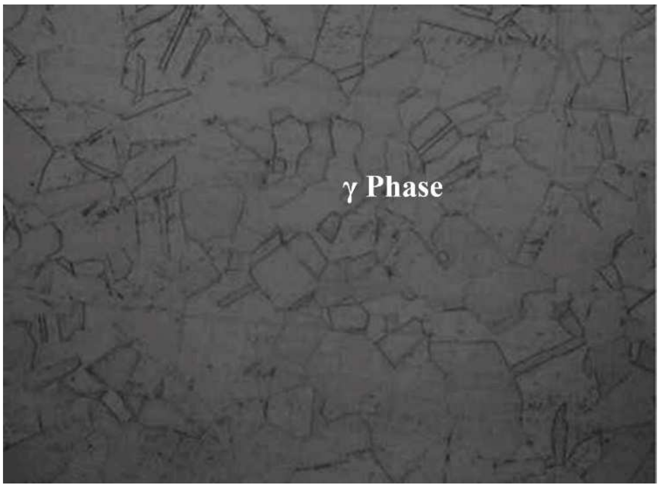

(a)

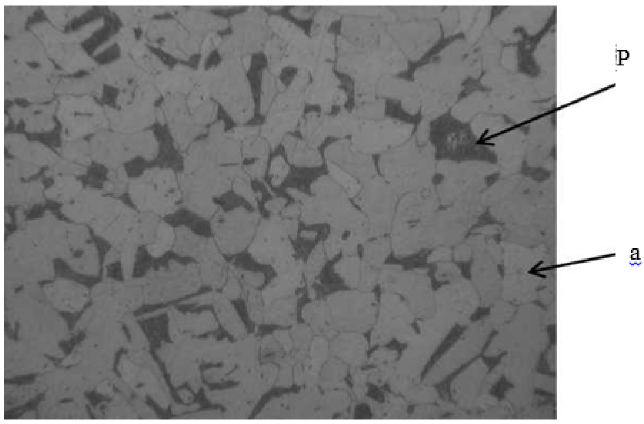

(b)

Fig. 1. a) Microstructure of stainless steel (x200); b) Microstructure of carbon steel (x200) [77]

According to ASTM standards given in Table IV, austenitic stainless steel has relatively higher strength, yield strength, and elongation than carbon steel. The increased durability limit of austenitic steel is due to the nickel content of about 8%. The element Ni not only has the effect of stabilizing austenite at normal temperatures but also improves the durability, ductility, and toughness of the steel.

TABLE IV
MECHANICAL PROPERTIES OF STAINLESS STEEL AND CARBON STEEL

Type	Strength (MPa)	Yield limit (MPa)	Relative elongation (%)
Stainless steel	>515	>205	>40
Carbon steel	>415	240	30

When welding stainless steel with carbon steel, the microstructure of the welding metal changes. The main factors affecting the change in microstructure include the chemical composition of the material, temperature, and cooling rate [78,79]. The weld is divided into the following zones: melting zone (also known as the weld metal zone after crystallization), transition zone at the carbon steel border, heat-affected zone on the carbon steel side, and transition zone on the outside. stainless steel side, stainless steel side heat affected zone, and original base metal zone [80]. Fig. 2 shows an overview diagram of the division of regions in a weld of two dissimilar materials.

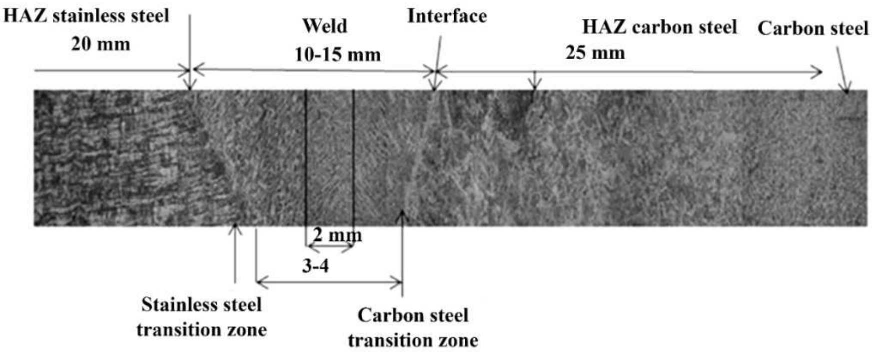

Fig. 2 Overview diagram of the structure of the weld between stainless steel and carbon steel [77]

The weld metal region (also known as the molten region or weld pool region) consists of the electrode metal and the base metal in a completely liquid state after crystallization to form a weld joint. The structure in this region is δ-ferrite on an austenite base.

The transition zone is a small area limited by the fusion boundary and the weld zone [81–83]. Here, electrode metal and molten base metal are mixed. If the chemical composition of the electrode and the base metal is equivalent (e.g., on the stainless-steel side), it is difficult to determine the size of this region. The concentration difference can be determined using the EDS line if it is significant. The HAZ is calculated from the melting boundary to the temperature zone of 500ºC. Different from the stainless-steel side, the structure changes a lot on the carbon-steel side compared to the organization of the original base metal. During the process of welding two different materials, under the effect of the welding arc, the electrode metal and base metal will melt, then the liquid metal will undergo a crystallization process to form a welding bond. [84,85]. The fluid flow and heat transfer greatly influence the properties of the weld metal in the weld pool. Liquid metal flow is affected by the following factors: surface tension, buoyancy, and electromagnetic force when current flows through [86,87]. Welding gas dynamics also significantly impact the convection process of liquid metal in the weld pool. The buoyancy effect will lead to spatial variation of liquid metal density, mainly by temperature changes over a smaller range, creating local mixing in this region. The influence of the electromagnetic field is a consequence of the interaction between the distributed current in the weld pool and the generated magnetic field. The contact of the driving force to the weld pool surface can be the leading cause of flow dynamics [88,89]. Fluid flow, convection, and heat transfer are often crucial in determining the weld pool's size and shape, the weld's microstructure and macrostructure, and the material's weldability.

Under the influence of physical processes, in the outermost boundary layer of liquid metal, substances will be mixed from the electrode metal and the base metal in a ratio of 80 - 20%, called the "unmixed zone". The redistribution of substances here is mainly due to the movement of liquid flow and solutes in the liquid alloy. The diffusion distance of the elements is called the “thickness of the solute layer at the boundary zone”. The transition zone observed at the fusion boundary of carbon steel is a region where the concentration of elements changes from the weld metal to the base metal. In the experiment, the EDS-line method cutting through the carbon steel melting boundary on the weld cross-section is used to determine the size of this region and the distribution curve of alloying elements. The experimental measurement results are shown in Fig. 3.

It can be seen from Fig. 3 that the distribution curve of the alloying elements is divided into three distinct regions: the horizontal region on the left has the content of the elements coinciding with the content of the electrode metal; The horizontal area on the right has an elemental content identical to that of carbon steel; The transition zone is the area in between where the content of elements changes. The width of this region is measured to be 80μm. In particular, the content of Fe element gradually increases, and the content of Cr and Ni gradually decreases from the carbon steel side to the weld metal side.

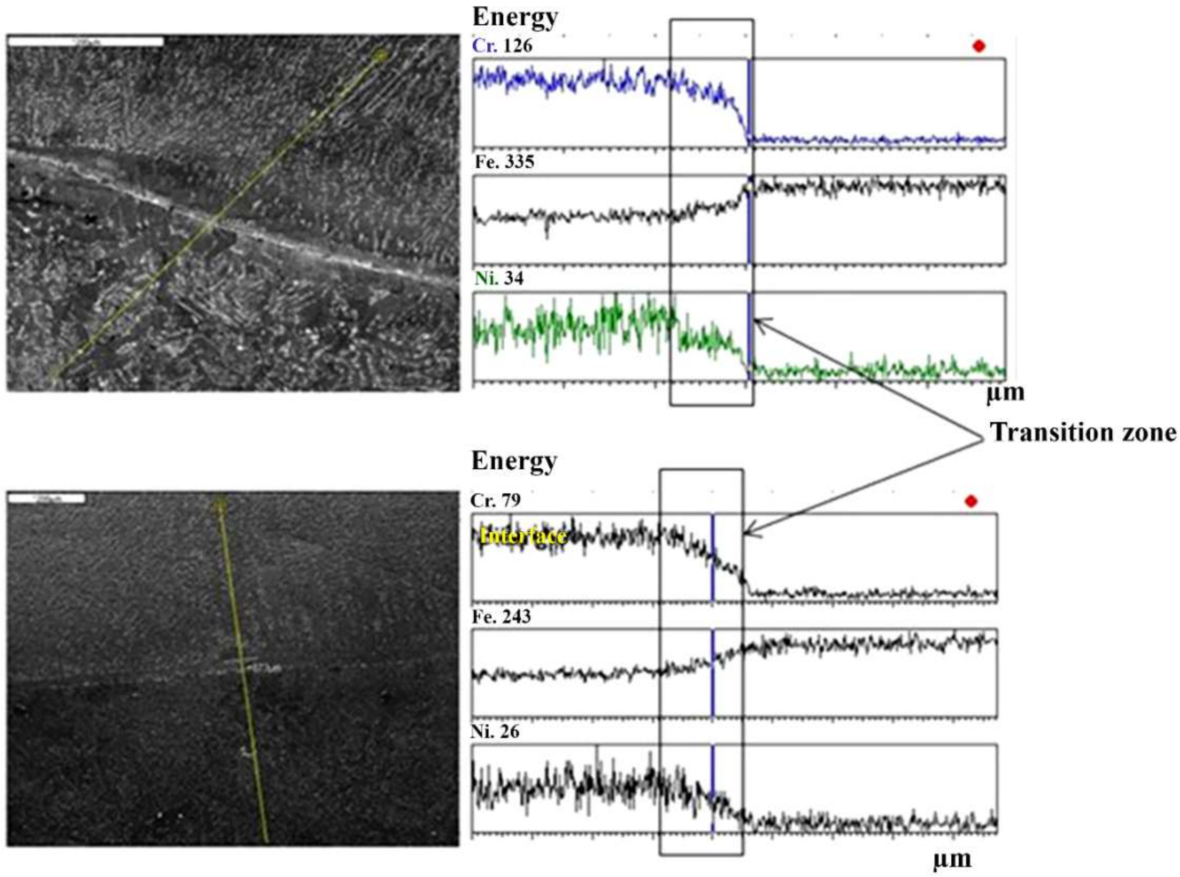

Fig. 3 Concentration distribution curves of elements in the transition zone [77]

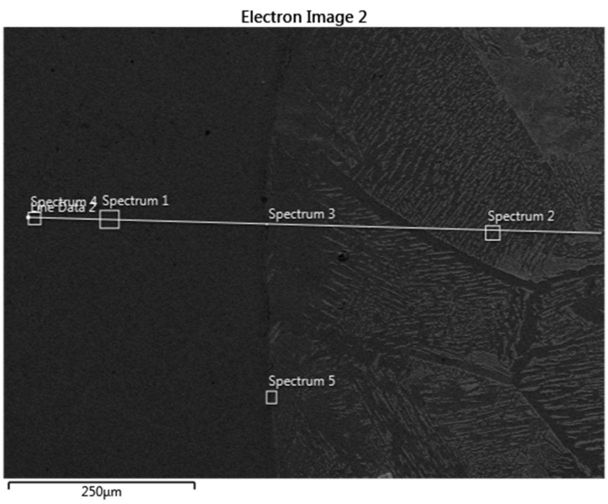

(a)

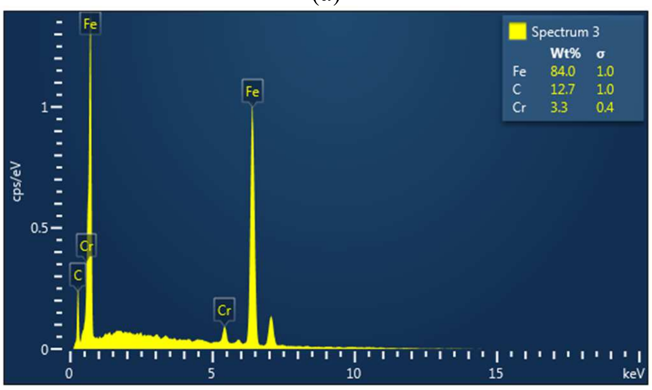

(b)

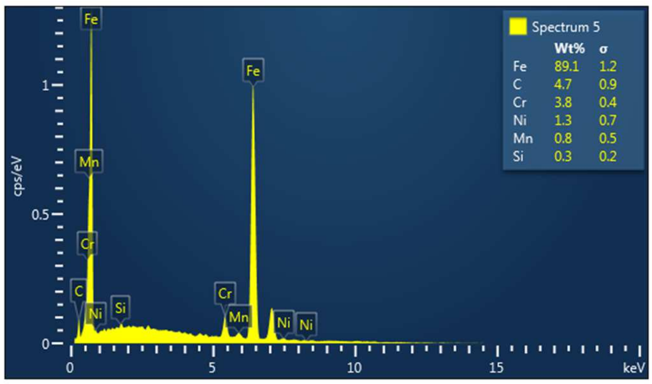

(c)

Fig. 4 Chemical composition at the carbon steel melting boundary; a) SEM analysis of EDS points, b) Results of analysis of EDS points 3, c) Results of analysis of EDS points 5 [77]

However, at different locations on the melting boundary, the element distribution curves are different. For example, at measurement point 3 in Fig. 4(a-c), the content of alloying elements is 3.3%Cr, 0%Ni; but at measurement point 5, the content of alloying elements is 3.8%Cr, 1.3%Ni, 0.8%Mo, 0.3%Si. The change in the content of alloying elements affected the thickness of the Martensite layer formed at the boundary. The structure area on the weld metal side is obtained as a completely Austenitic area 5-20µm wide (white area running along the border), followed by the δ - Ferrite structure on the Austenite base. Besides, the black region running along the melting boundary is predicted to be a completely Martensitic region. However, the size of the

Martensite layer is not uniform, ranging from 2 to 10µm, as shown in Fig. 5.

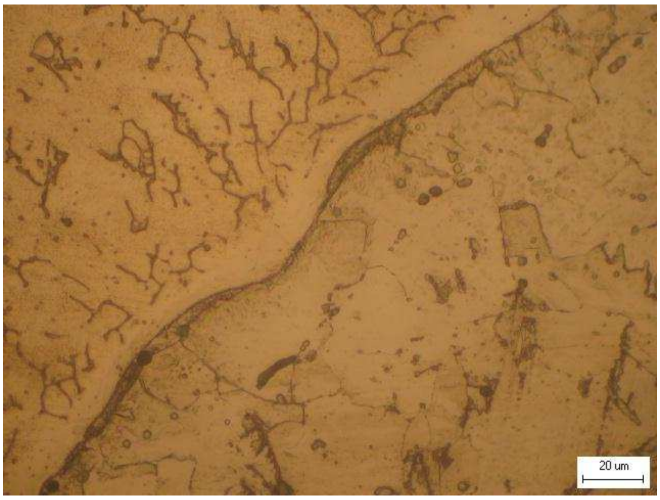

Fig. 5 Microstructure at carbon steel melting boundary (x500) [77]

The formation of a martensite layer with a variable width from 5 - 10µm along the molten border of the weld metal is a combination of the rapid cooling rate of the welding process and the local chemical composition at the molten border. In the area adjacent to the base metal, a stable layer of Austenite exists during the welding process, so during the cooling process, because the cooling speed in this area is very high, the temperature drops rapidly from the Austenitization temperature T ~ T_{solid} to normal temperature T_o = 30ºC, so according to the CCT diagram, a part of Austenite transforms into martensite. The transformation process begins to occur when the temperature is lower than the transformation starting temperature Ms. The Ms value can be determined based on the composition of the alloying elements.

With low alloy steel (content of alloying elements less than 5%):

$$M_s = 561 - 474\%C - 33\%Mn - 17\%Cr - 17\%Ni - 21\%Mo \quad (1)$$

With alloy steel (chromium content less than 14%)

$$M_s = 635 - 474\%C - 33\%Mn - 17\%Cr - 17\%Ni - 21\%Mo \quad (2)$$

With stainless steel:

$$M_s = 502 - 810\%C - 13\%Mn - 12\%Cr - 30\%Ni - 6\%Mo \quad (3)$$

The width of the martensitic layer varies along the melt boundary which can be explained by the concentration difference of the alloying elements. At the molten boundary layer, there exists a layer of metal whose composition of elements continuously changes from the base metal to the electrode metal [90]. The difference in concentration gradient at the locations leads to different Ms temperatures. Therefore, the width of the martensite layers will vary depending on the location. It could be seen the microstructure of steel at the molten boundary with a magnification of 1000 times in Fig. 6.

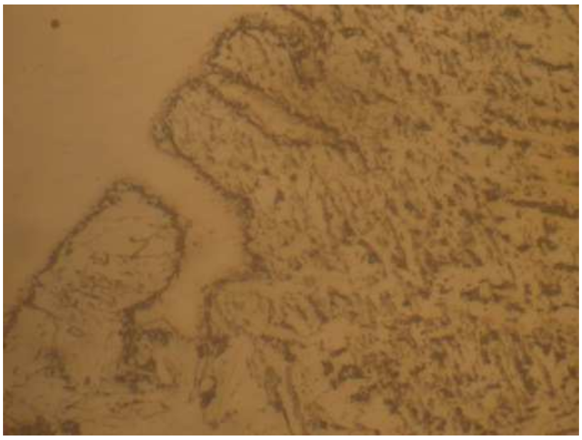

(a)

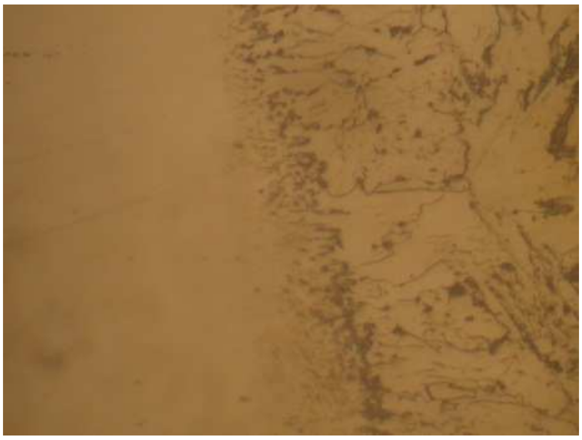

(b)

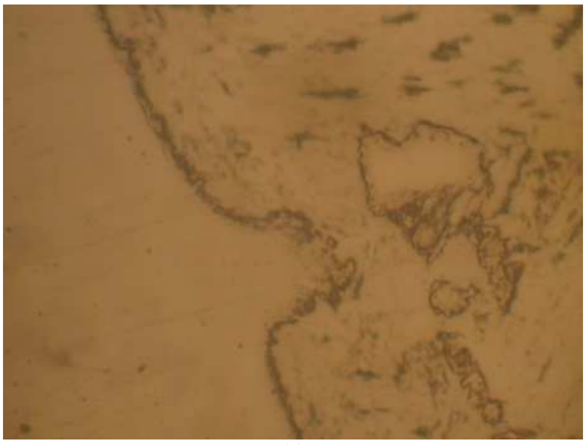

(c)

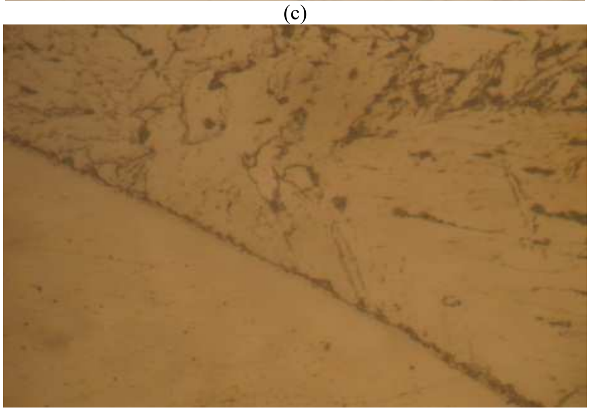

(d)

Fig. 6 Molten boundary shape change (x1000 times) [77]

Mixing in the transition zone causes the formation of boundary layer separation as well as the change in the shape of the molten boundary layer. There are four types of organization, as shown in Fig. 6. The transition zone in terms of composition has a change in composition. This is the cause of the formation of carbon from the base metal to the metal electrodes when working at high temperatures [91]. The Martensite layer is a hard and brittle phase, running along the melt boundary and forming a clear separation between the base metal and the electrode metal [92]. This may be the area where cracks and destruction appear under long-term working conditions [77].

B. Influence of microstructure formation on the properties of the transition zone

Considering the change in hardness in the transition zone, according to the hardness value given in Table V, the hardness at the molten boundary layer is the largest up to 390HV. This is completely appropriate because a Martensite layer is formed here running along the carbon steel molten border. Martensite is a hard and brittle phase, so the hardness is high.

TABLE V
HARDNESS VALUES AT THE TRANSITION ZONE ON THE CARBON STEEL SIDE

Position	Border	Welding materials		Carbon steel	
Distance from the melting boundary (µm)	0	100	200	100	200
Hardness (HV)	390	173	160	146	134

Considering the tensile test results, all test specimens were not destroyed at the transition zone. Although the formation of Martensite is a hard and brittle phase between soft phases, the width of this region is very small (about 5 - 10µm), so it does not affect the overall mechanical properties of the entire weld.

C. Influence of the input heat field on the diffusion ability of elements forming the weld

The welding heat source affects the diffusion ability of weld metal elements, thereby forming a structure in the weld. The welding heat source is evaluated through the line energy dq and this value depends on the welding parameters. Kou et al. [25] pointed out that, as the line energy increases, the shape of the weld pool will be elongated, changing from an ellipse to a droplet shape, and this change in shape is also different for each type of material. Line energy also significantly affects the structure of the weld metal area and the HAZ [76]. In the 202 austenitic stainless-steel welds, when the line energy is small, the δ - ferrite in the weld metal region is small in size, and the distance between the branches is small and vice versa. In the HAZ, the greater the line energy, the greater the width of the HAZ. The size of the particles in this region is also proportional to the line energy. Many different views have been given regarding the influence of line energy on the mechanical properties of welds. Some studies have shown that as line energy increases, microhardness in the weld metal and HAZ increases, tensile strength increases, and impact toughness decreases. [93–95]. However, in some cases, hardness and tensile strength decrease with increasing line energy. The cause is the formation of carbides or the creation of brittle and unstable phases in the HAZ of the material [96,97].

Determining the maximum temperature curve plays an important role in calculating the cooling rate, and the width of the heat-affected zone as well as predicting the organization in the HAZ zone of the weld. Maximum temperature is the highest temperature at each location on the HAZ area achieved during the welding process [98–100]. From the Rossenthal equation, the maximum temperature at each point is determined by finding the extrema for Eq. (4) for thin plates and Eq. (5) for thick plates.

- With thin plate (2D):

$$T_p - T_0 = \left(\frac{2}{\pi e}\right)^{1/2} \frac{q/v}{d\rho c 2r} \tag{4}$$

- With thick plate (3D):

$$T_p - T_0 = \left(\frac{2}{\pi e}\right) \frac{q/v}{\rho c r^2} \tag{5}$$

where Tp comprises the maximum temperature at a distance r from the heat source, (ºC). Ramy et al. [101] determined the influence of heat input and residual stress on fatigue crack propagation. For this study, they created a finite element model and showed that changing the heat input will change RS distribution, welding deformation, and weld penetration. However, the shift in welding HI did not have a significant effect on the magnitude of the welding induction, as shown in Fig. 7.

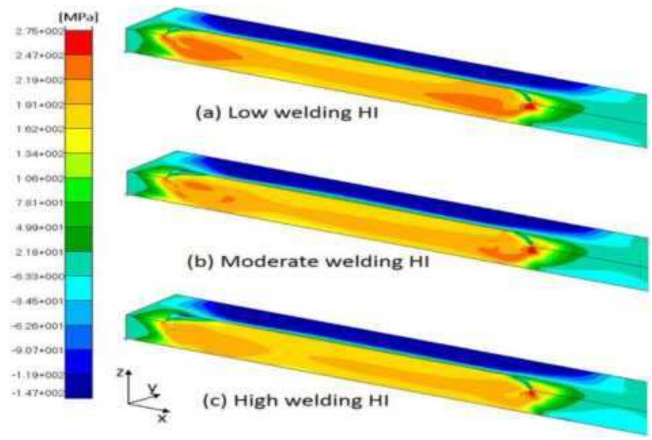

Fig. 7 Effect of change in heat input on weld line distribution [101]

Jinfeng et al. [102] studied the effect of energy input on the mechanical and microstructural properties of laser welded DP1000 steel and they concluded that as the input energy decreased, the weld line width and the softening zone shrinks and there is an increase in mechanical properties as the energy input decreases. The study further shows that as the energy input increases, the grain of this zone becomes coarse, and the mechanical properties of the weld become poorer, as depicted in Fig. 8.

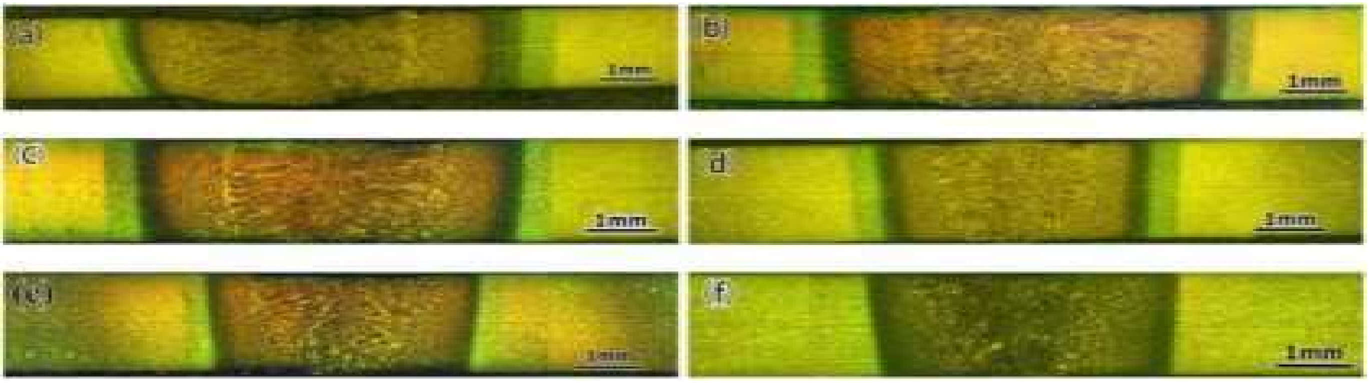

Fig. 8 Division of welding zone structure when (a) Input energy is 325 J/mm; (b) Input energy is 217 J/mm; (c) Input energy is 163 J/mm; (d) input energy is 130J/mm; (e) input energy is 108 J/mm and (f) input energy is 93 J/mm [102]

Leonardo et al. [103] determined the heat input effect on the properties of an AA5052 friction stir weld and observed an increase in power with diameter, as well as a lower level of defects in the stirring line. Hardness also decreases with tool diameter, due to higher thermal effects on the microstructure, as shown in Fig. 9.

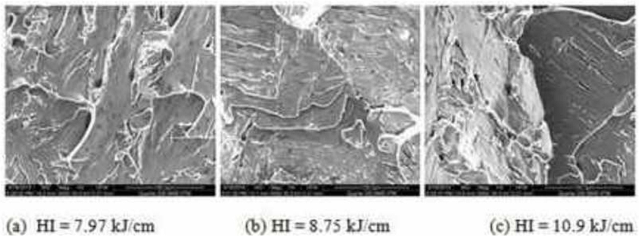

Fig. 9 SEM images of the weld deposition impact test surface under different heat inputs [103]

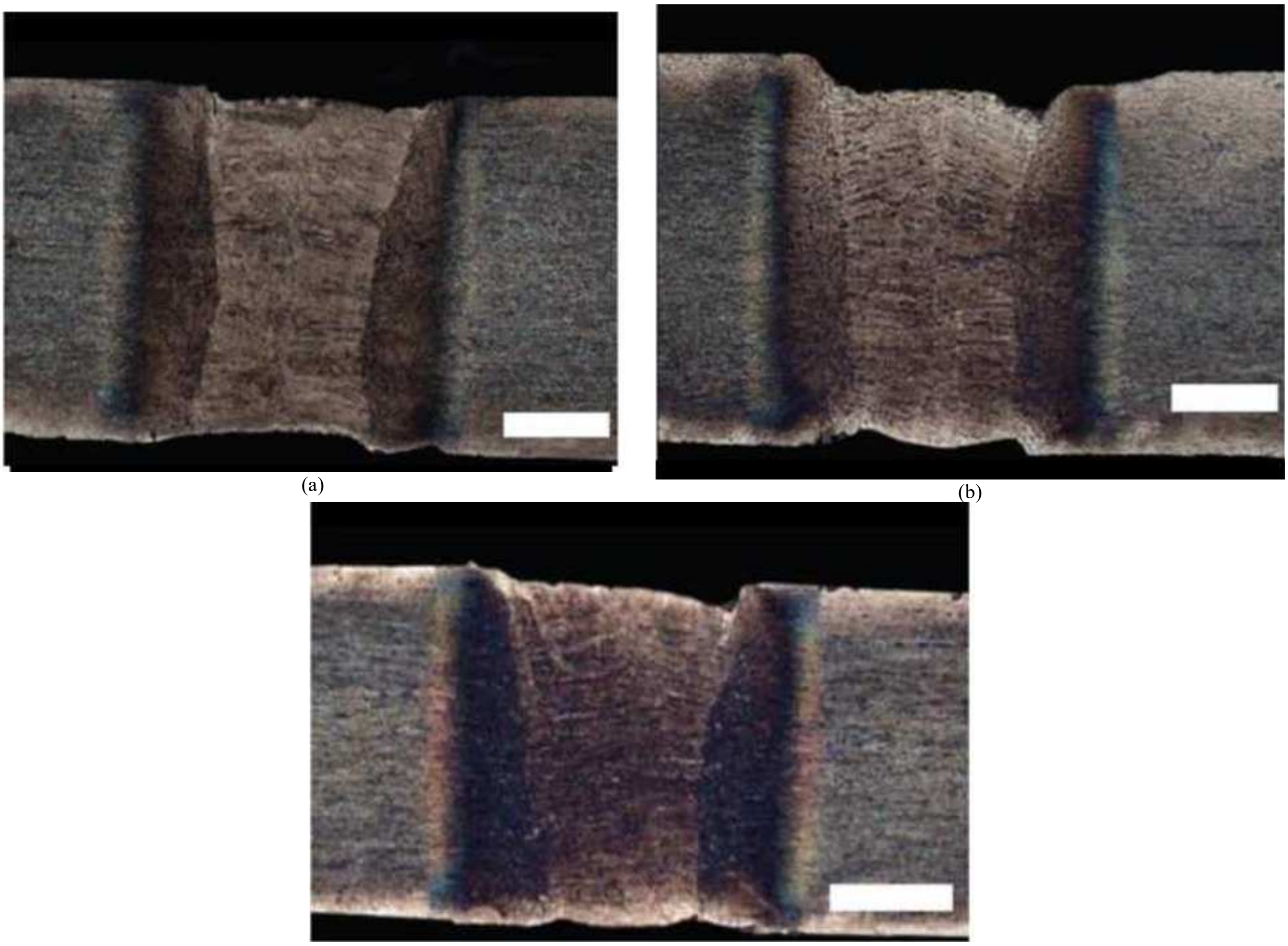

Fig. 10 Microstructure of the weld joint with a process heat input of 0.051 kJ/mm (a); 0.043 kJ/mm (b); 0.037 kJ/mm (c) [106]

Chellappan et al. [104] studied the effect of heat input on the mechanical and microstructural properties of AISI 410S martensitic stainless steel welds, welded using the GTAW method. Gao et al. [105] studied the effect of heat input on the mechanical and microstructural properties of pulsed laser welds in Ti6Al4V/Nb, two different alloys, they concluded that when there is an increase in heat input, the width of the HAZ at the Ti6Al4V edge increases significantly and the filling defects move out of the melt zone. The mechanical properties as well as the microstructure and inhomogeneity of the weld in the fusion zone increase as the heat input increases. Adam et al. [106] studied the effect of heat input on the hardness distribution and microstructure of steel welded with Si-Al alloy by laser method. For this study, the authors considered applied heat input values of 0.037-0.053 kJ/mm and the results obtained showed no significant impact on the microstructure and microhardness of the laser molten metal area. While the HAZ and melt zone sizes increase with increasing heat input as well as the fact that a heat input of 0.051 kJ/mm is responsible for the excessive grain growth, the value of this parameter must be limited to about 0.045 kJ/mm, as shown in Fig. 10.

Lichan et al. [107] determined the effect of welding heat input on the microstructure and grain size of 316L SS welds. Zhang et al. [108] studied the effect of heat input on the mechanical and microstructural properties of DSS welds welded using the EBW process. The results show that increasing heat input will promote the growth of grain boundary austenite and the formation of fine austenite inside the grain. EB has significantly higher microhardness than BM, and EB welds have relatively lower strength than BM when varying the value of heat input, as depicted in Fig. 11.

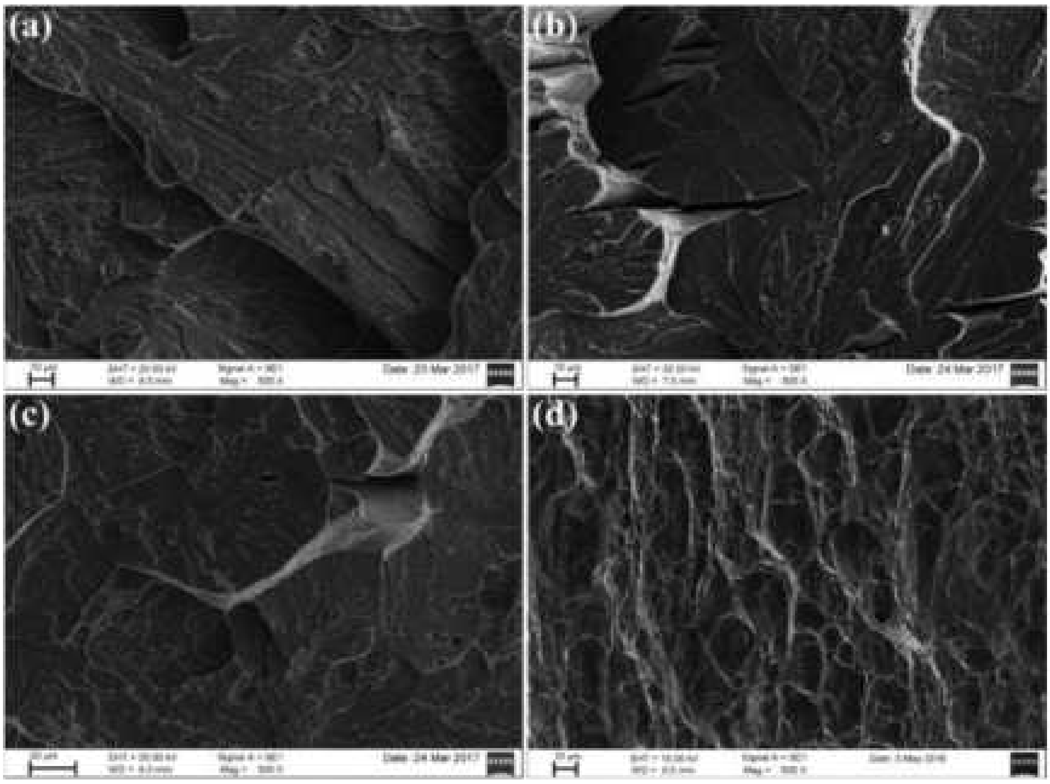

Fig. 11 SEM images of EB welds with different heat inputs of (a) 0.43, (b) 0.46, (c) 0.50 kJ/mm, and (d) BM [106]

IV. Conclusions

The change in microstructure after welding is limited around the fusion zone and HAZ zone, which is the main reason for the inhomogeneity in mechanical properties between the zones and the process of diffusion phase transformation during heat treatment. Based on the crystallization mechanism, the liquid phase transition (corresponding to the melting zone) and the solid phase transition mechanism (corresponding to the HAZ zone) are used to explain the organization obtained in the zones. The transition zone between the solid base metal and the completely liquid metal region has three factors simultaneously changing: the mixing of the chemical composition of the elements, the morphology of the solid/liquid phase interface, and the crystallization model. The concentration gradient is small on the stainless-steel side, so the crystallization model is FA. The HAZ is the region with the lowest mechanical properties partly due to the appearance of hard and brittle phases such as Vidmantes Ferrite, Bainite, and Martensite. These phases are products of the austenitic transformation process upon continuous cooling under the influence of the maximum temperature at points during the welding process, the difference in cooling rate, and the concentration gradient. Martensitic bands appear along the fusion boundary reaching the largest value in the entire weld, at about 390-400HV.

REFERENCES

[1] Vo D-T, Nguyen D-N, Nguyen T-D, Nguyen X-P, Said Z, Nguyen D-T. Influence of diffusion mode on microstructure and mechanical properties of carbonitriding layer. 2022 Adv. Sci. Eng. Technol. Int. Conf., IEEE; 2022, p. 1–7. doi: 10.1109/ASET53988.2022.9734917.

[2] Pham X., Hoang A., Nguyen D. A study on the effect of the change of tempering temperature on the microstructure transformation of Cu-Ni-Sn alloy. Int J Mech Mechatronics Eng 2018;18:27–34.

[3] Nguyen DN, Hoang AT, Pham XD, Sai MT, Chau MQ, Pham V V. Effect of sn component on properties and microstructure CU-NI-SN alloys. J Teknol 2018;80:43–51. doi:10.11113/jt.v80.11867.

[4] Kluczyk M, Grządziela A, Batur T. Design and Operational Diagnostics of Marine Propellers Made of Polymer Materials. Polish Marit Res 2022;29:115–22. doi:10.2478/pomr-2022-0049.

[5] Kowalski J, Kozak J. Influence of Material Thickness on the Ductile Fracture of Steel Plates for Shipbuilding. Polish Marit Res 2022;29:160–6. doi:10.2478/pomr-2022-0036.

[6] Kazymyrenko Y, Solomoniuk N, Drozd O. Glass Microspheres Thermo-Deformation Sintering Processes in the Technologies of Obtaining Materials for Underwater Technical Equipment. Polish Marit Res 2023;30:174–80. doi:10.2478/pomr-2023-0050.

[7] Nguyen VN, Nguyen AX, Nguyen DT, Le HC, Nguyen VP. A Comprehensive Understanding of Bainite Phase Transformation Mechanism in TRIP Bainitic-supported Ferrite Steel. Int J Adv Sci Eng Inf Technol 2024;14:309–25. doi:10.18517/ijaseit.14.1.19706.

[8] Pham XD, Hoang AT, Nguyen DN, Le VV. Effect of factors on the hydrogen composition in the carburizing process. Int J Appl Eng Res 2017;12:8238–8244.

[9] Hoang A., Nguyen D., Pham V. Heat treatment furnace for improving the weld mechanical properties: Design and fabrication. Int J Mech Eng Technol 2018;9:496–506.

[10] Pham MK, Nguyen DN, Hoang AT. Influence of vanadium content on the microstructure and mechanical properties of high-manganese steel. Int J Mech Mechatronics Eng 2018;18:141–147.

[11] Hoang AT, Tran TT Van, Nguyen VB, Nguyen DN. Effect of Heat Treatment Process on The Microstructure and Mechanical Properties of The Spray Coating Ni-Cr on CT38 Steel. Int J Adv Sci Eng Inf Technol 2019;9:560–8. doi:10.18517/ijaseit.9.2.7891.

[12] Xuan Tran T, Phuong Nguyen X, Nam Nguyen D, Toai Vu D, Quang Chau M, Ibrahim Khalaf O, et al. Effect of Poly-Alkylene-Glycol Quenchant on the Distortion, Hardness, and Microstructure of 65Mn Steel. Comput Mater Contin 2021;67:3249–64. doi:10.32604/cmc.2021.015411.

[13] Vo D-T, Nguyen D-N, Sai M-T, Said Z, Nguyen X-P, Nguyen D-T. A study of microstructure and properties of Cu-Ni-Sn alloy when deformation and aging. 2022 Adv. Sci. Eng. Technol. Int. Conf., IEEE; 2022, p. 1–6.

[14] Tuan Hoang A, Phuong Nguyen X, Ibrahim Khalaf O, Xuan Tran T, Quang Chau M, Minh Hao Dong T, et al. Thermodynamic Simulation on the Change in Phase for Carburizing Process. Comput Mater Contin 2021;68:1129–45. doi:10.32604/cmc.2021.015349.

[15] Abid M, Kchaou M, Hoang AT, Haboussi M. Wear Mechanisms Analysis and Friction Behavior of Anodic Aluminum Oxide Film 5083 under Cyclic Loading. J Mater Eng Perform 2024;33:1527–1537. doi:10.1007/s11665-023-08616-8.

[16] Wang Y, Chen X, Konovalov S V. Additive manufacturing based on welding arc: a low-cost method. J Surf Investig X-Ray, Synchrotron Neutron Tech 2017;11:1317–28.

[17] Singh R. Applied welding engineering: processes, codes, and standards. Butterworth-Heinemann; 2020.

[18] Karayel E, Bozkurt Y. Additive manufacturing method and different welding applications. J Mater Res Technol 2020;9:11424–38.

[19] Wang B, Hu SJ, Sun L, Freiheit T. Intelligent welding system technologies: State-of-the-art review and perspectives. J Manuf Syst 2020;56:373–91.

[20] Khedr M, Hamada A, Järvenpää A, Elkatatny S, Abd-Elaziem W. Review on the Solid-State Welding of Steels: Diffusion Bonding and Friction Stir Welding Processes. Metals (Basel) 2022;13:54. doi:10.3390/met13010054.

[21] Serindağ HT, Çam G. Characterizations of Microstructure and Properties of Dissimilar AISI 316L/9Ni Low-Alloy Cryogenic Steel Joints Fabricated by Gas Tungsten Arc Welding. J Mater Eng Perform 2023;32:7039–49. doi;10.1007/s11665-022-07601-x.

[22] Laska A, Szkodo M. Manufacturing Parameters, Materials, and Welds Properties of Butt Friction Stir Welded Joints–Overview. Materials (Basel) 2020;13:4940. doi:10.3390/ma13214940.

[23] Chang J, Cao R, Yan Y. The joining behavior of titanium and Q235 steel joined by cold metal transfer joining technology. Materials (Basel) 2019;12. doi:10.3390/ma12152413.

[24] Lee CH, Chang KH. Temperature fields and residual stress distributions in dissimilar steel butt welds between carbon and stainless steels. Appl Therm Eng 2012;45–46. doi:10.1016/j.applthermaleng.2012.04.007.

[25] Welding metallurgy and weldability of stainless steels. Choice Rev Online 2005;43. doi:10.5860/choice.43-2230.

[26] Shi H, Chen K, Liang Z, Dong F, Yu T, Dong X, et al. Intermetallic compounds in the banded structure and their effect on mechanical properties of Al/Mg dissimilar friction stir welding joints. J Mater Sci Technol 2017;33:359–66.

[27] Sonar T, Balasubramanian V, Malarvizhi S, Venkateswaran T, Sivakumar D. An overview on welding of Inconel 718 alloy-Effect of welding processes on microstructural evolution and mechanical properties of joints. Mater Charact 2021;174:110997.

[28] Zhou Q, Liu R, Ran C, Fan K, Xie J, Chen P. Effect of microstructure on mechanical properties of titanium-steel explosive welding interface. Mater Sci Eng A 2022;830:142260.

[29] Umar M, Sathiya P. Influence of melting current pulse duration on microstructural features and mechanical properties of AA5083 alloy weldments. Mater Sci Eng A 2019;746:167–78.

[30] Zhang J, Xin W, Luo G, Wang R, Meng Q. Significant influence of welding heat input on the microstructural characteristics and mechanical properties of the simulated CGHAZ in high nitrogen V-alloyed steel. High Temp Mater Process 2020;39:33–44.

[31] Pankaj P, Tiwari A, Biswas P. Impact of varying tool position on the intermetallic compound formation, metallographic/mechanical characteristics of dissimilar DH36 steel, and aluminum alloy friction stir welds. Weld World 2021:1–33.

[32] Verma J, Taiwade RV. Effect of welding processes and conditions on the microstructure, mechanical properties and corrosion resistance of duplex stainless steel weldments—A review. J Manuf Process 2017;25:134–52. doi:10.1016/j.jmapro.2016.11.003.

[33] Dak G, Pandey C. A critical review on dissimilar welds joint between martensitic and austenitic steel for power plant application. J Manuf Process 2020;58:377–406. doi:10.1016/j.jmapro.2020.08.019.

[34] Dunđer M, Vuherer T, Samardžić I, Marić D. Analysis of heat-affected zone microstructures of steel P92 after welding and after post-weld heat treatment. Int J Adv Manuf Technol 2019;102:3801–12. doi:10.1007/s00170-019-03513-8.

[35] Yamagishi H. High-Productivity and High-Strength Fe/Al and Al/Al Dissimilar Joining by Spot Forge-Welding. Metall Mater Trans A 2021;52:741–52. doi:10.1007/s11661-020-06118-z.

[36] Kumar N, Pandey C, Kumar P. Dissimilar Welding of Inconel Alloys With Austenitic Stainless-Steel: A Review. J Press Vessel Technol 2023;145. doi:10.1115/1.4055329.

[37] Jabar S, Barenji AB, Franciosa P, Kotadia HR, Ceglarek D. Effects of the adjustable ring-mode laser on intermetallic formation and mechanical properties of steel to aluminium laser welded lap joints. Mater Des 2023;227:111774.

[38] Cheng Z, Ye Z, Huang J, Yang J, Chen S, Zhao X. Influence of heat input on the intermetallic compound characteristics and fracture mechanisms of titanium-stainless steel MIG-TIG double-sided arc welding joints. Intermetallics 2020;127:106973.

[39] David SA, Deevi SC. Welding of unique and advanced ductile intermetallic alloys for high-temperature applications. Sci Technol Weld Join 2017;22:681–705.

[40] Tao T, Zhou D, Liu J, Wang X. Improvement of laser welded joint properties of AZ31B magnesium alloy to DP590 dual-phase steel produced by external magnetic field. J Manuf Process 2022;79:270–83.

[41] Le TN, Pham MK, Hoang AT, Bui, TNM, Nguyen DN. Microstructure change for multi-pass welding between Austenitic stainless steel and carbon steel. J Mech Eng Res Dev 2018;41:97–102. doi:10.26480/jmerd.02.2018.97.102.

[42] Saadati M, Nobarzad AKE, Jahazi M. On the hot cracking of HSLA steel welds: Role of epitaxial growth and HAZ grain size. J Manuf Process 2019;41:242–51.

[43] Cabrilo A, Geric K. Fracture mechanic and charpy impact properties of a crack in weld metal, HAZ and base metal of welded armor steel. Procedia Struct Integr 2018;13:2059–64.

[44] Cao R, Feng Z, Chen JH. Microstructures and properties of titanium-copper lap welded joints by cold metal transfer technology. Mater Des 2014;53. doi:10.1016/j.matdes.2013.06.030.

[45] Tomashchuk I, Sallamand P, Belyavina N, Pilloz M. Evolution of microstructures and mechanical properties during dissimilar electron

beam welding of titanium alloy to stainless steel via copper interlayer. Mater Sci Eng A 2013;585. doi:10.1016/j.msea.2013.07.050.
[46] Chu Q, Zhang M, Li J, Yan C, Qin Z. Influence of vanadium filler on the properties of titanium and steel TIG welded joints. J Mater Process Technol 2017;240. doi:10.1016/j.jmatprotec.2016.06.018.
[47] He P, Zhang J, Zhou R, Li X. Diffusion bonding technology of a titanium alloy to a stainless steel web with an Ni interlayer. Mater Charact 1999;43. doi:10.1016/S1044-5803(99)00008-X.
[48] Tomashchuk I, Sallamand P, Andrzejewski H, Grevey D. The formation of intermetallics in dissimilar Ti6Al4V/copper/AISI 316 L electron beam and Nd:YAG laser joints. Intermetallics 2011;19. doi:10.1016/j.intermet.2011.05.016.
[49] Hao X, Dong H, Li S, Xu X, Li P. Lap joining of TC4 titanium alloy to 304 stainless steel with fillet weld by GTAW using copper-based filler wire. J Mater Process Technol 2018;257. doi:10.1016/j.jmatprotec.2018.02.020.
[50] Yao C, Xu B, Zhang X, Huang J, Fu J, Wu Y. Interface microstructure and mechanical properties of laser welding copper-steel dissimilar joint. Opt Lasers Eng 2009;47. doi:10.1016/j.optlaseng.2009.02.004.
[51] Zhao Y, Wang W, Yan K, Liu C, Zou J. Microstructure and properties of Cu/Ti laser welded joints. J Mater Process Technol 2018;257. doi:10.1016/j.jmatprotec.2018.03.001.
[52] Chen S, Zhang M, Huang J, Cui C, Zhang H, Zhao X. Microstructures and mechanical property of laser butt welding of titanium alloy to stainless steel. Mater Des 2014;53. doi:10.1016/j.matdes.2013.07.044.
[53] Magnabosco I, Ferro P, Bonollo F, Arnberg L. An investigation of fusion zone microstructures in electron beam welding of copper-stainless steel. Mater Sci Eng A 2006;424. doi:10.1016/j.msea.2006.03.096.
[54] Huang J, He X, Guo Y, Zhang Z, Shi Y, Fan D. Joining of aluminum alloys to galvanized mild steel by the pulsed DE-GMAW with the alternation of droplet transfer. J Manuf Process 2017;25. doi:10.1016/j.jmapro.2016.10.003.
[55] Sun QJ, Li JZ, Liu YB, Li BP, Xu PW, Feng JC. Microstructural characterization and mechanical properties of Al/Ti joint welded by CMT method—Assisted hybrid magnetic field. Mater Des 2017;116. doi:10.1016/j.matdes.2016.12.025.
[56] Zhou X, Zhang G, Shi Y, Zhu M, Yang F. Microstructures and mechanical behavior of aluminum-copper lap joints. Mater Sci Eng A 2017;705. doi:10.1016/j.msea.2017.08.056.
[57] Cao R, Chang JH, Huang Q, Zhang XB, Yan YJ, Chen JH. Behaviors and effects of Zn coating on welding-brazing process of Al-Steel and Mg-steel dissimilar metals. J Manuf Process 2018;31. doi:10.1016/j.jmapro.2018.01.001.
[58] Kang Y, Park G, Jeong S, Lee C. Correlation Between Microstructure and Low-Temperature Impact Toughness of Simulated Reheated Zones in the Multi-pass Weld Metal of High-Strength Steel. Metall Mater Trans A 2018;49:177–86. doi:10.1007/s11661-017-4384-3.
[59] Zhang Z, Jing H, Xu L, Han Y, Li G, Zhao L. Investigation on Microstructure and Impact Toughness of Different Zones in Duplex Stainless Steel Welding Joint. J Mater Eng Perform 2017;26:134–50. doi:10.1007/s11665-016-2441-5.
[60] Li S, Li J, Sun G, Deng D. Modeling of welding residual stress in a dissimilar metal butt-welded joint between P92 ferritic steel and SUS304 austenitic stainless steel. J Mater Res Technol 2023;23. doi:10.1016/j.jmrt.2023.02.123.
[61] Bezawada S, Gajjela R. Microstructural and Mechanical Characterization of Welded Joints between Stainless Steel and Hastelloy Made Using Pulsed Current Gas Tungsten Arc Welding. J Mater Eng Perform 2023;32. doi:10.1007/s11665-022-07197-2.
[62] Wang B, Qiu F, Chen L, Zhou Q, Dong B, Yang H, et al. Microstructure and shearing strength of stainless steel/low carbon steel joints produced by resistance spot welding. J Mater Res Technol 2022;20. doi:10.1016/j.jmrt.2022.08.041.
[63] Shen J, Gonçalves R, Choi YT, Lopes JG, Yang J, Schell N, et al. Microstructure and mechanical properties of gas metal arc welded CoCrFeMnNi joints using a 308 stainless steel filler metal. Scr Mater 2023;222. doi:10.1016/j.scriptamat.2022.115053.
[64] Wang J, Lu MX, Zhang L, Chang W, Xu LN, Hu LH. Effect of welding process on the microstructure and properties of dissimilar weld joints between low alloy steel and duplex stainless steel. Int J Miner Metall Mater 2012;19. doi:10.1007/s12613-012-0589-z.
[65] Safari M, Mostaan H, Derakhshan E. Microstructual and mechanical studies of the dissimilar tabular joints of Incoloy alloy 825 and AISI 316 stainless steel. J Mar Eng Technol 2020;19. doi:10.1080/20464177.2018.1508805.
[66] Ibrahim IR, Khedr M, Mahmoud TS, Abdel-Aleem HA, Hamada A. Study on the mechanical performance of dissimilar butt joints between low Ni medium-Mn and Ni-Cr austenitic stainless steels processed by gas tungsten arc welding. Metals (Basel) 2021;11. doi:10.3390/met11091439.
[67] Chuaiphan W, Srijaroenpramong L. Effect of hydrogen in argon shielding gas for welding stainless steel grade SUS 201 by GTA welding process. J Adv Join Process 2020;1. doi:10.1016/j.jajp.2020.100016.
[68] Zhang H, Xu J, Hao D, Esmail OMAO. Microstructure and Mechanical Properties of Laser-Welded Joints between DP590 Dual-Phase Steel and 304 Stainless Steel with Preset Nickel Coating. Materials (Basel) 2023;16. doi:10.3390/ma16072774.
[69] Chen HC, Ng FL, Du Z. Hybrid laser-TIG welding of dissimilar ferrous steels: 10 mm thick low carbon steel to 304 austenitic stainless steel. J Manuf Process 2019;47. doi:10.1016/j.jmapro.2019.10.013.
[70] Azwinur, Syukran, Akhyar, Ferdiyansyah. The Effect of Electrode Type on The Tensile Strength Characteristics of Welded Joints Between SA.240 Tp.304 Stainless Steel and SA.36 Carbon Steel Alloys through SMAW Welding Process. Int J Integr Eng 2022;14. doi:10.30880/ijie.2022.14.04.004.
[71] Gope DK, Chattopadhyaya S. Dissimilar Welding of Nickel Based Superalloy with Stainless Steel: Influence of Post Weld Heat Treatment. Mater Manuf Process 2022;37. doi:10.1080/10426914.2021.1945095.
[72] García-García V, Frasco-García OD, Reyes-Calderón F, Hernández-Cristóbal O, Vergara-Hernández HJ. Effect of the thermal field on the microstructure of dissimilar welded joints between TWIP steel and 2205 duplex stainless steel. J Mater Res Technol 2022;17. doi:10.1016/j.jmrt.2022.02.029.
[73] Hajiannia I, Shamanian M, Kasiri M. Microstructure and mechanical properties of AISI 347 stainless steel/A335 low alloy steel dissimilar joint produced by gas tungsten arc welding. Mater Des 2013;50. doi:10.1016/j.matdes.2013.03.029.
[74] Khan M, Dewan MW, Sarkar MZ. Effects of welding technique, filler metal and post-weld heat treatment on stainless steel and mild steel dissimilar welding joint. J Manuf Process 2021;64. doi:10.1016/j.jmapro.2021.02.058.
[75] Nhung LT, Khanh PM, Hai LM, Nam ND. The relationship between continuous cooling rate and microstructure in the heat affected zone (HAZ) of the dissimilar weld between carbon steel and austenitic stainless steel. Acta Metall Slovaca 2017;23. doi:10.12776/ams.v23i4.1002.
[76] Hoang AT, Le V V, Nguyen AX, Nguyen DN. A Study On The Changes In Microstructure And Mechanical Properties Of Multi-Pass Welding Between 316 Stainless Steel And Low-Carbon Steel. J Adv Manuf Technol 2018;12:25–40.
[77] Nhung LT. Investigation the changes of microstructures and properties of the dissimilar welds between carbon steel and austenitic stainless steel. Hanoi University of Science and Technology, 2020.
[78] Liu FC, Hovanski Y, Miles MP, Sorensen CD, Nelson TW. A review of friction stir welding of steels: Tool, material flow, microstructure, and properties. J Mater Sci Technol 2018;34:39–57. doi:10.1016/j.jmst.2017.10.024.
[79] Prabakaran MP, Kannan GR, Pandiyarajan R. Effects of Welding Speed on Microstructure and Mechanical Properties of CO2 Laser Welded Dissimilar Butt Joints between Low Carbon Steel and Austenitic Stainless Steel. Adv Mater Process Technol 2022;8:1–12. doi:10.1080/2374068X.2020.1855960.
[80] Le TN, Pham MK, Hoang AT, Nguyen DN. Microstructures And Elements Distribution In The Transition Zone Of Carbon Steel And Stainless Steel Welds. J Mech Eng Res Dev 2018;41:27–31. doi:10.26480/jmerd.03.2018.27.31.
[81] Zhou X, Zhao H, Liu F, Yang B, Chen B, Tan C. Influence of energy ratio on microstructure and mechanical properties in the transition zone of hybrid laser-MIG welded AH36/316L dissimilar joints. J Mater Res Technol 2021;15:4487–501.
[82] Hu YN, Wu SC, Chen L. Review on failure behaviors of fusion welded high-strength Al alloys due to fine equiaxed zone. Eng Fract Mech 2019;208:45–71.
[83] Ishigami A, Roy MJ, Walsh JN, Withers PJ. The effect of the weld fusion zone shape on residual stress in submerged arc welding. Int J Adv Manuf Technol 2017;90:3451–64.
[84] Kang H, Sharma A, Jung JP. Recent Progress in Transient Liquid Phase and Wire Bonding Technologies for Power Electronics. Metals (Basel) 2020;10:934. doi:10.3390/met10070934.
[85] Xu T, Shi Y, Cui Y, Liang Z. Effects of Magnetic Fields in Arc Welding, Laser Welding, and Resistance Spot Welding: A Review.

Adv Eng Mater 2023;25. doi:10.1002/adem.202200682.
[86] Xing C, Jia C, Han Y, Dong S, Yang J, Wu C. Numerical Analysis of the Metal Transfer and Welding Arc Behaviors in Underwater Flux-cored Arc Welding. Int J Heat Mass Transf 2020;153:119570. doi:10.1016/j.ijheatmasstransfer.2020.119570.
[87] Cho W-I, Na S-J. Impact of driving forces on molten pool in gas metal arc welding. Weld World 2021;65:1735–47. doi:10.1007/s40194-021-01138-8.
[88] Ngo Huu M, Nguyen Van A, Nguyen Van T, Tran Hai D, Nguyen Van T, Nguyen Tien D, et al. Material Flow Behavior on Weld Pool Surface in Plasma Arc Welding Process Considering Dominant Driving Forces. Appl Sci 2020;10:3569. doi:10.3390/app10103569.
[89] Luo M, Hu R, Li Q, Huang A, Pang S. Physical understanding of keyhole and weld pool dynamics in laser welding under different water pressures. Int J Heat Mass Transf 2019;137:328–36. doi:10.1016/j.ijheatmasstransfer.2019.03.129.
[90] Oliveira JP, Santos TG, Miranda RM. Revisiting fundamental welding concepts to improve additive manufacturing: From theory to practice. Prog Mater Sci 2020;107:100590. doi:10.1016/j.pmatsci.2019.100590.
[91] Huang Y, Huang J, Zhang J, Yu X, Li Q, Wang Z, et al. Microstructure and corrosion characterization of weld metal in stainless steel and low carbon steel joint under different heat input. Mater Today Commun 2021;29:102948. doi:10.1016/j.mtcomm.2021.102948.
[92] Gürol U. Welding of High Manganese Austenitic Cast Steels Using Stainless Steel Covered Electrode. Int J Met 2023;17:1021–33. doi:10.1007/s40962-022-00834-5.
[93] West P, Shunmugasamy VC, Usman CA, Karaman I, Mansoor B. Part II.: Dissimilar friction stir welding of nickel titanium shape memory alloy to stainless steel – microstructure, mechanical and corrosion behavior. J Adv Join Process 2021;4:100072. doi:10.1016/j.jajp.2021.100072.
[94] Moravec J, Novakova I, Sobotka J, Neumann H. Determination of Grain Growth Kinetics and Assessment of Welding Effect on Properties of S700MC Steel in the HAZ of Welded Joints. Metals (Basel) 2019;9:707. doi:10.3390/met9060707.
[95] Qi X, Du L, Hu J, Misra RDK. Enhanced impact toughness of heat affected zone in gas shield arc weld joint of low-C medium-Mn high strength steel by post-weld heat treatment. Steel Res Int 2018;89:1700422.
[96] Chen S, Zhao L bin, Wang J, Li C, Li Z, Ye X-X, et al. Microstructure evolution and mechanical properties of simulated HAZ in a Ni-17Mo-7Cr superalloy: effects of the welding thermal cycles. J Mater Sci 2020;55:13372–88. doi:10.1007/s10853-020-04927-6.
[97] Jeong S, Lee Y, Park G, Kim B, Moon J, Park S-J, et al. Phase transformation and the mechanical characteristics of heat-affected zones in austenitic Fe–Mn–Al–Cr–C lightweight steel during post-weld heat treatment. Mater Charact 2021;177:111150. doi:10.1016/j.matchar.2021.111150.
[98] Wei C, Zhang J, Yang S, Tao W, Wu F, Xia W. Experiment-based regional characterization of HAZ mechanical properties for laser welding. Int J Adv Manuf Technol 2015;78:1629–40.
[99] Sharma SK, Maheshwari S, Singh RKR. Modeling and optimization of HAZ characteristics for submerged arc welded high strength pipeline steel. Trans Indian Inst Met 2019;72:439–54.
[100] Garcia MP, Gervasyev A, Lu C, Barbaro FJ. Chemical composition and weld cooling time effects on heat-affected zone hardness of line pipe steels. Int J Press Vessel Pip 2022;200:104837.
[101] Gadallah R, Osawa N, Tanaka S, Tsutsumi S. Critical investigation on the influence of welding heat input and welding residual stress on stress intensity factor and fatigue crack propagation. Eng Fail Anal 2018;89. doi:10.1016/j.engfailanal.2018.02.028.
[102] Wang J, Yang L, Sun M, Liu T, Li H. Effect of energy input on the microstructure and properties of butt joints in DP1000 steel laser welding. Mater Des 2016;90. doi:10.1016/j.matdes.2015.11.006.
[103] Tufaro LN, Manzoni I, Svoboda HG. Effect of Heat Input on AA5052 Friction Stir Welds Characteristics. Procedia Mater Sci 2015;8. doi:10.1016/j.mspro.2015.04.152.
[104] Muthusamy C, Karuppiah L, Paulraj S, Kandasami D, Kandhasamy R. Effect of heat input on mechanical and metallurgical properties of gas tungsten arc welded lean super martensitic stainless steel. Mater Res 2016;19. doi:10.1590/1980-5373-MR-2015-0538.
[105] Gao XL, Liu J, Zhang LJ. Effect of heat input on microstructure and mechanical properties of pulsed laser welded joints in Ti6Al4V/Nb dissimilar alloys. Int J Adv Manuf Technol 2018;94. doi:10.1007/s00170-017-1134-z.
[106] Grajcar A, Różański M, Stano S, Kowalski A, Grzegorczyk B. Effect of heat input on microstructure and hardness distribution of laser welded Si-Al TRIP-type steel. Adv Mater Sci Eng 2014;2014. doi:10.1155/2014/658947.
[107] Li LC, Chai MY, Li YQ, Bai WJ, Duan Q. Effect of welding heat input on grain size and microstructure of 316L stainless steel welded joint. Appl. Mech. Mater., vol. 331, 2013. doi:10.4028/www.scientific.net/AMM.331.578.
[108] Huang H, Fan G, Tan Z, Xiong DB, Guo Q, Guo C, et al. Superplastic behavior of carbon nanotube reinforced aluminum composites fabricated by flake powder metallurgy. Mater Sci Eng A 2017;699:55–61. doi:10.1016/j.msea.2017.05.074.